Volume 15
Number 5
7 February 2023
Pages 1965-2438

# Nanoscale

rsc.li/nanoscale

ISSN 2040-3372

ROYAL SOCIETY OF CHEMISTRY

**COMMUNICATION**
Bin Yu, Xin He, Fei Xue *et al.*
Piezoelectricity-modulated optical recombination dynamics of monolayer-$MoS_2$/GaN-film heterostructures

NCNST

Nanoscale

ROYAL SOCIETY OF CHEMISTRY

COMMUNICATION

View Article Online
View Journal | View Issue



Cite this: *Nanoscale*, 2023, **15**, 2036

Received 21st October 2022,
Accepted 3rd December 2022

DOI: 10.1039/d2nr05850b

rsc.li/nanoscale



# Piezoelectricity-modulated optical recombination dynamics of monolayer-$MoS_2$/GaN-film heterostructures†

Baoyu Wang,[a] Jr-Hau He,[b] Bin Yu, *[a] Xin He *[a] and Fei Xue *[a]

**Dynamic manipulation of optoelectronic responses by mechanical stimuli is promising for developing wearable electronics and human–machine interfacing. Although 2D–3D hybrid heterostructures can bring advancements in optoelectronics, their dynamic optical responses to external strains remain rarely studied. Here, we demonstrate the strain-tuned recombination dynamics of monolayer-$MoS_2$ and thin-film-GaN heterostructures. We find that optical excitons in the heterostructures, apart from trions, can be markedly modulated by strains. We argue that $MoS_2$ piezoelectric dipoles across the interfaces lead to curved band diagrams, in which optical excitons dissociate into spatially separated quasiparticles and concurrently relocate to the maxima of valence bands and the minima of conduction bands. With the increase in tensile strains, the photoluminescence (PL) intensity of the heterostructures shows quenched responses. Noticeably, the change in PL spectra strongly depends on the directions of the applied strains because of the lateral piezoelectric periodicity of $MoS_2$ flakes. This work not only helps in understanding the underlying physics of the decreased PL intensities upon applying strains but also demonstrates a feasible way (*i.e.*, strains) to manipulate the PL efficiency of 2D-material-based optoelectronics.**

Two-dimensional (2D) materials, including ultrathin $MoS_2$, exhibit remarkable physical properties, unlike those of the bulk. For example, monolayer $MoS_2$ pertains to a $D_{3h}$ space group and lacks inversion symmetry;[1,2] the Coulomb interaction between electrons and holes is largely enhanced in monolayer $MoS_2$.[3] Furthermore, a direct bandgap of ~1.85 eV, which lies in the spectral range of visible light, endows monolayer $MoS_2$ with intriguing optical properties.[4–8] A broad range of ultrathin $MoS_2$ optoelectronics have been developed, including photodetectors,[9–15] photovoltaics,[16–19] LEDs,[20–24] and photoelectrochemical cells.[25,26] Monolayer $MoS_2$ features a hexagonal crystal structure and it is non-centrosymmetric, thus demonstrating strong piezoelectricity along the $e_{11}$ direction.[27] Unfortunately, piezoelectricity emerges only from odd-numbered layers of $MoS_2$ crystals but disappears in even-numbered layers.[28,29] Moreover, piezoelectric-$MoS_2$-based self-adaptive piezophototronic devices offer a possible way to develop flexible nano-opto-electromechanical systems.[30,31] The inherent piezoelectricity (*i.e.*, piezoelectric field), triggered by a high-frequency acoustic wave, has been used to tune the photoluminescence (PL) efficiency of monolayer $MoS_2$ grown on a sapphire substrate.[32]

2D-material-based heterostructures provide a new platform for exploring rich physics and device applications. Vertical stacking of ultrathin $MoS_2$ semiconductors with traditional bulk materials has received considerable attention due to the combination of both 2D and 3D merits.[33–35] The 2D–3D assembly can not only help us to realize high-performance electronics/optoelectronics but also overcome technological challenges in silicon scaling.[20,36,37] Using the piezoelectricity of ZnO thin films, the photocurrent in a $MoS_2$–ZnO 2D–3D heterojunction photodiode has been enhanced four times by the piezophototronic effect.[38] However, to date, whether the strain-induced piezoelectric field in heterostructures such as monolayer $MoS_2$ could regulate photo-excited dynamic responses in these vertically integrated 2D–3D heterostructures remains rarely studied.

Monolayer $MoS_2$ shows a small lattice mismatch with GaN films,[39] and the hybrid of these two materials is promising for high-performance optoelectronics. Here, using the vertically stacked monolayer-$MoS_2$/GaN-film heterostructures as a model system, we study the piezoelectricity-modulated carrier recombination dynamics. Compared to separate monolayer $MoS_2$, the PL spectra of the heterostructures show a remarkably decreased weight of trion $X^-$ and exciton B, which is associated with charge transfer over the interfaces. When tensile strains

[a]*ZJU-Hangzhou Global Scientific and Technological Innovation Center, School of Micro-Nano Electronics, Zhejiang University, Hangzhou 310020, China. E-mail: yu-bin@zju.edu.cn, xin.he@kaust.edu.sa, xuef@zju.edu.cn*
[b]*Department of Materials Science and Engineering, City University of Hong Kong, Hong Kong SAR, China*

† Electronic supplementary information (ESI) available. See DOI: https://doi.org/10.1039/d2nr05850b

are applied to the heterostructures, the 2S-Mo piezoelectric dipoles lead to a bent energy band. The excitons dissociate into spatially separated quasi-particles and are stored in the maxima and minima of valence and conduction bands. Accordingly, with the increase of in-plane strain magnitude, the PL peaks related to $MoS_2$ distinctly decrease and the variation strongly depends on the in-plane directions of the applied strain due to the periodic in-plane $MoS_2$ piezoelectricity. This work helps us to illustrate the underlying physical mechanisms of strain-dependent quenching of PL spectra for 2D heterostructure optoelectronics.

## Evolution of the Raman and PL spectra at different temperatures

As shown in Fig. 1a, exfoliated n-type $MoS_2$ flakes on silica substrates were transferred to p-type GaN films, forming vertically stacked p–n 3D–2D heterostructures. Temperature-dependent Raman spectra were used to study the evolution of heterostructure photon vibration. In Fig. 1b, typical Raman signals of p-type GaN films at room temperature are presented to help identify the origin of the whole heterostructure spectra. Two strong Raman peaks, located at 570 $cm^{-1}$ and 735 $cm^{-1}$, are observed because of the contributions from $E_2$ and $A_1$ longitudinal optical modes in GaN films.[40] Moreover, a small peak is detected at 418 $cm^{-1}$, which originates from the sapphire substrate as previously reported.[41] Fig. 1c shows the temperature-dependent Raman spectra for monolayer-$MoS_2$/GaN heterostructures. It is seen that Raman responses from the heterostructures are superimposed by those from $MoS_2$ flakes and GaN films. Raman scattering intensities of in-plane $E_{2g}{}^1$ and out-of-plane $A_{1g}{}^1$ modes associated with $MoS_2$ flakes are relatively weak and the width between those active modes remains 19 $cm^{-1}$, which is in agreement with previous works.[42,43] With the increase in temperature, all Raman peaks exhibit a redshift and the width for $E_{2g}{}^1$ and $A_{1g}{}^1$ remains constant as shown in Fig. 1c and S1.† The temperature-induced variation at the Raman peak position is mainly attributed to thermal expansion.[44] To systematically examine the variation of photon vibration for heterostructures with different layered $MoS_2$, the temperature-dependent Raman spectra acquired for four-layer-$MoS_2$/GaN and bulk-$MoS_2$/GaN heterostructures are shown in Fig. 1d and e. As highlighted in Fig. 1d and e, the widths of two significant $MoS_2$ peaks are 23 $cm^{-1}$ and 25 $cm^{-1}$ for four-layer and bulk heterostructures, respectively. When the temperatures are dramatically increased, the redshift trends for the two heterostructures coincide with that for monolayer-$MoS_2$/GaN heterostructures. It is noted that compared to the Raman spectra shown in Fig. 1c, the emission peaks related to $MoS_2$ are largely intensified, while the peaks related to GaN film substrate weaken. This is caused by the increased thickness of $MoS_2$ and agrees with the variation of separate $MoS_2$.[44]

Next, we turn to the characterization of photoexcited dynamics of $MoS_2$/GaN heterostructures by PL spectra. For

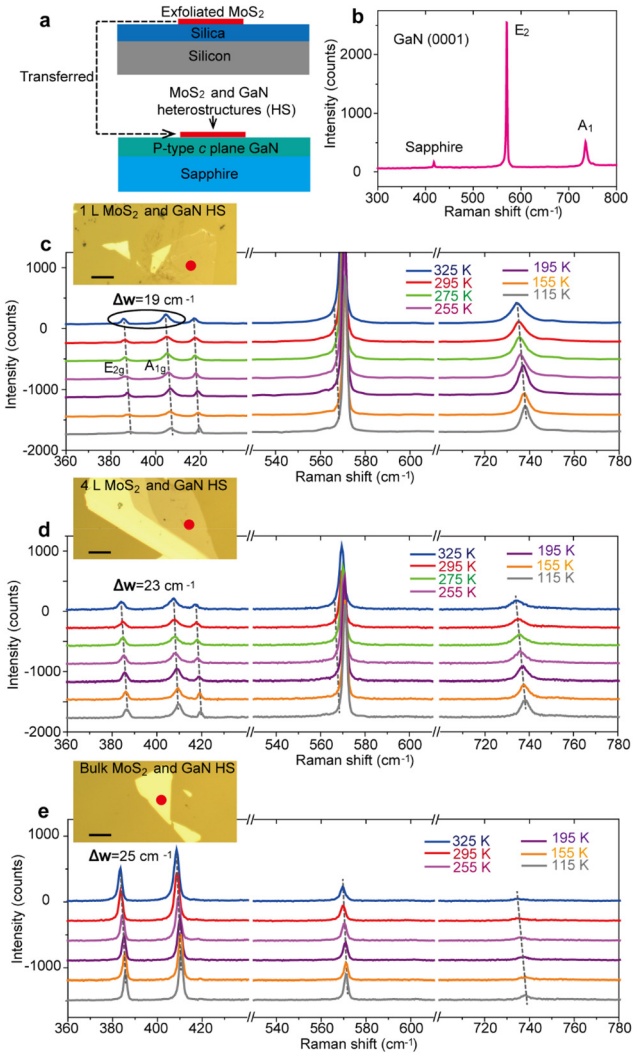


**Fig. 1** Raman spectra of $MoS_2$/GaN heterostructures. (a) Schematics of the fabrication of vertically stacked $MoS_2$/GaN heterostructures. Exfoliated $MoS_2$ flakes on silica were transferred to the GaN film by a wet chemical method. (b) Typical Raman spectra for GaN films with the *c* plane at room temperature. Temperature-dependent Raman spectra obtained for the heterostructures consisting of (c) 1-layer, (d) 4-layer, and (e) bulk $MoS_2$. With the increase in temperature, all Raman active peaks exhibit a red shift. Raman spectra were excited by a 532 nm laser and the red dots in the insets of (c)–(e) represent the photoexcited spots. Scale bar: 10 μm.

comparison, Fig. 2a shows the PL responses of separate monolayer $MoS_2$ on silica substrates. Due to the strong spin–orbit coupling in monolayer $MoS_2$, valence bands at the K points of the Brillouin zone can split, giving rise to two prominent direct-bandgap transitions (*i.e.*, excitons A and B) as shown in the inset of Fig. 2a.[2] Experimentally, the PL spectra of monolayer $MoS_2$ exhibit two significant peaks (A and B). However, reduced dielectric screening in a monolayer crystal facilitates enhanced Coulomb interaction between holes and electrons. Thus, tightly bound excitons or trions with high binding energy easily form,[45] which dominate the optical properties of

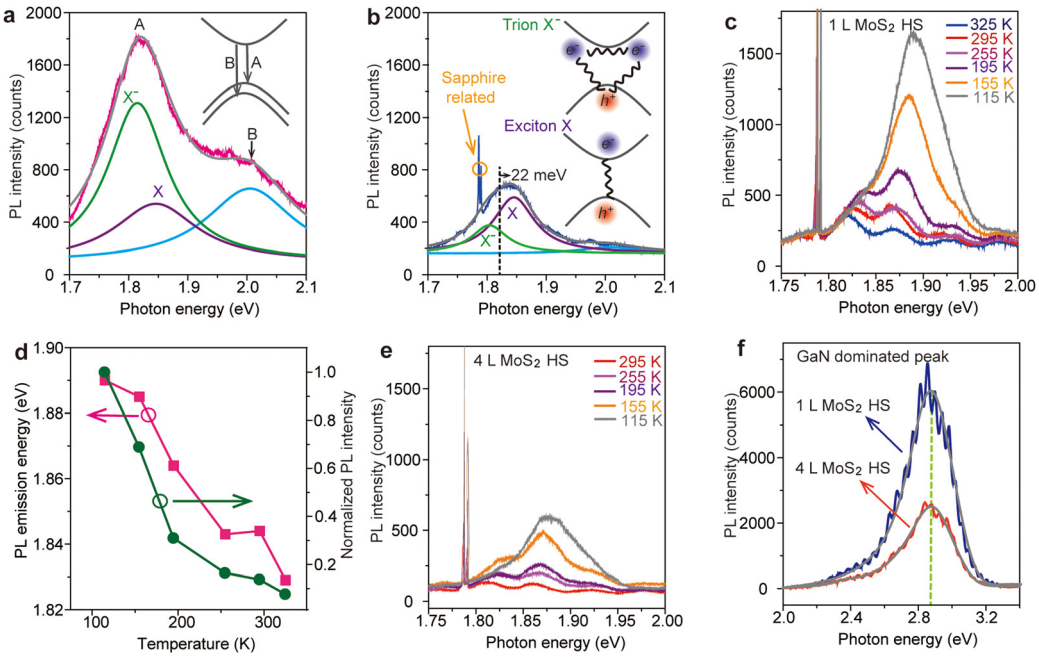


**Fig. 2** PL spectra of typical $MoS_2$/GaN heterostructures. PL responses at ~1.8 eV, which were collected from (a) separate monolayer $MoS_2$ on silica substrates and (b) monolayer-$MoS_2$/GaN heterostructures using a 100× objective lens at room temperature. The inset in (a) shows A and B excitons generated by valence band splitting in monolayer $MoS_2$, whereas the schematics of excitons and trions are shown in the inset of (b). PL spectra were deconvoluted to show the change in neutral excitons (X), charged trions ($X^-$), and neutral excitons (B) using Lorentzian functions. Temperature-dependent PL spectra (c) and the relevant derived features (d), such as peak energy and peak height of the 1-layer-$MoS_2$/GaN heterostructure. The oscillating PL signals described here were collected through a 50× objective lens in the measurement system. (e) PL spectra of the 4-layer-$MoS_2$/GaN heterostructures at different temperatures. (f) GaN-dominated PL spectra for the vertical heterostructures at room temperature. The fitting curves are indicated by the grey lines. The $MoS_2$-related emission peaks are excited by a 532 nm laser, while the GaN-related emission peak is excited by a 325 nm laser.

ultrathin $MoS_2$ flakes[3] and play an important role in the photo-excited processes as described below. Fig. 2b shows PL emission peaks between 1.7 and 2.1 eV from monolayer-$MoS_2$/GaN heterostructures, while the inset exhibits the schematic of exciton (X) and trion ($X^-$) creation in $MoS_2$ crystals. As indicated by the orange arrow, a sharp and strong PL signal at 1.78 eV denotes the sapphire-substrate-related emission peak (Fig. S2†). When the n-type monolayer $MoS_2$ and p-type GaN films are assembled, charge transfer inevitably occurs,[46] leading to a decreased PL emission (Fig. 2b). A small PL blueshift (~22 meV) can be detected, possibly arising from the doping effect from the GaN substrate.[47] To give a deep insight into the spectral changes shown in Fig. 2a and b, the emission peaks are decomposed into a negative trion ($X^-$), neutral exciton (X), and high-energy exciton peaks (B) through the Lorentzian function.[4] Compared to the PL spectra of separate monolayer $MoS_2$, it is apparent that the spectral weights of the negative trion $X^-$ and exciton B are greatly reduced (the weight of exciton B nearly becomes zero), while that of exciton X is increased. This confirms the presence of charge transfer between the n-type $MoS_2$ flake and the p-type GaN film.

To explore the evolution of exciton and trion recombination, the temperature-dependent PL spectra of monolayer-$MoS_2$/GaN heterostructures were collected (Fig. 2c). Note that during the measurement a long-focus lens (50× objective) was used to leave a large space for applying strains. PL signal oscillation, especially at high temperatures, possibly stems from the heat effect and the interference of light at the $MoS_2$/GaN interface. When the temperature is decreased, PL spectra exhibit a blueshift from 1.83 eV to 1.89 eV (Fig. 2d), which is associated with the lattice shrinking effect. The peak intensity is markedly increased owing to the enhanced exciton recombination as quantitatively presented in Fig. 2d (the data are derived from the fitting lines of Fig. 2c). Fig. S3† shows the fitting curves of the temperature-dependent PL spectra using the Lorentzian function. To discuss the $MoS_2$-thickness-dependent PL emission from $MoS_2$/GaN heterostructures, 4-layer-$MoS_2$ was adopted. It is observed that the PL intensity of 4-layer-$MoS_2$/GaN heterostructures at different temperatures (Fig. 2e) is greatly decreased compared with that of the monolayer $MoS_2$ counterparts (Fig. 2c). Furthermore, Fig. 2f and S4† show another PL emission peak between 2.0 and 3.3 eV for different-layer-$MoS_2$/GaN heterostructures, and this peak corresponds to GaN-dominated responses. The PL intensity is expectedly weakened, which contrasts with separate GaN samples without top $MoS_2$ layers and verifies charge transfer across the vertical heterostructures. Note that the peak oscillation stems from the Fabry–Perot optical interference within the GaN film.[48]

 

## External strain-tuned recombination dynamics

Next, we examine strain-dependent PL responses for monolayer-$MoS_2$/GaN heterostructures. In the experiment, one edge of the substrate was tightly clamped on a right-angle bracket using a hexagonal nut (Fig. 3a); heterostructure samples were placed just above the edge of the bracket to ensure that they could receive the maximum strain. A 3D stage with a resolution of 10 μm was used to drive another right-angle bracket to apply tensile strains on the samples. From the stage, the largest displacement distance ($D_{max}$) can be obtained to estimate the magnitude of the applied strains. Fig. 3b shows the optical image of our practical testing set-up. The strain direction orientation along one edge of the trigonal $MoS_2$ flake is defined as 0°, as indicated by the grey dashed arrow highlighted in the optical image of the monolayer-$MoS_2$/GaN heterostructure (the right inset shown in Fig. 3b). Fig. 3c plots PL responses with different tensile strains and strain directions (*e.g.*, 0° and 30°; the scenario of 45° is presented in Fig. S5†). As the strain magnitude increases, PL signals show a quenching behavior and a slight red shift induced by the piezoresistance effect. Note that the strain magnitude described here is much smaller than that applied to the flexible substrate, which is because 2D materials have a good

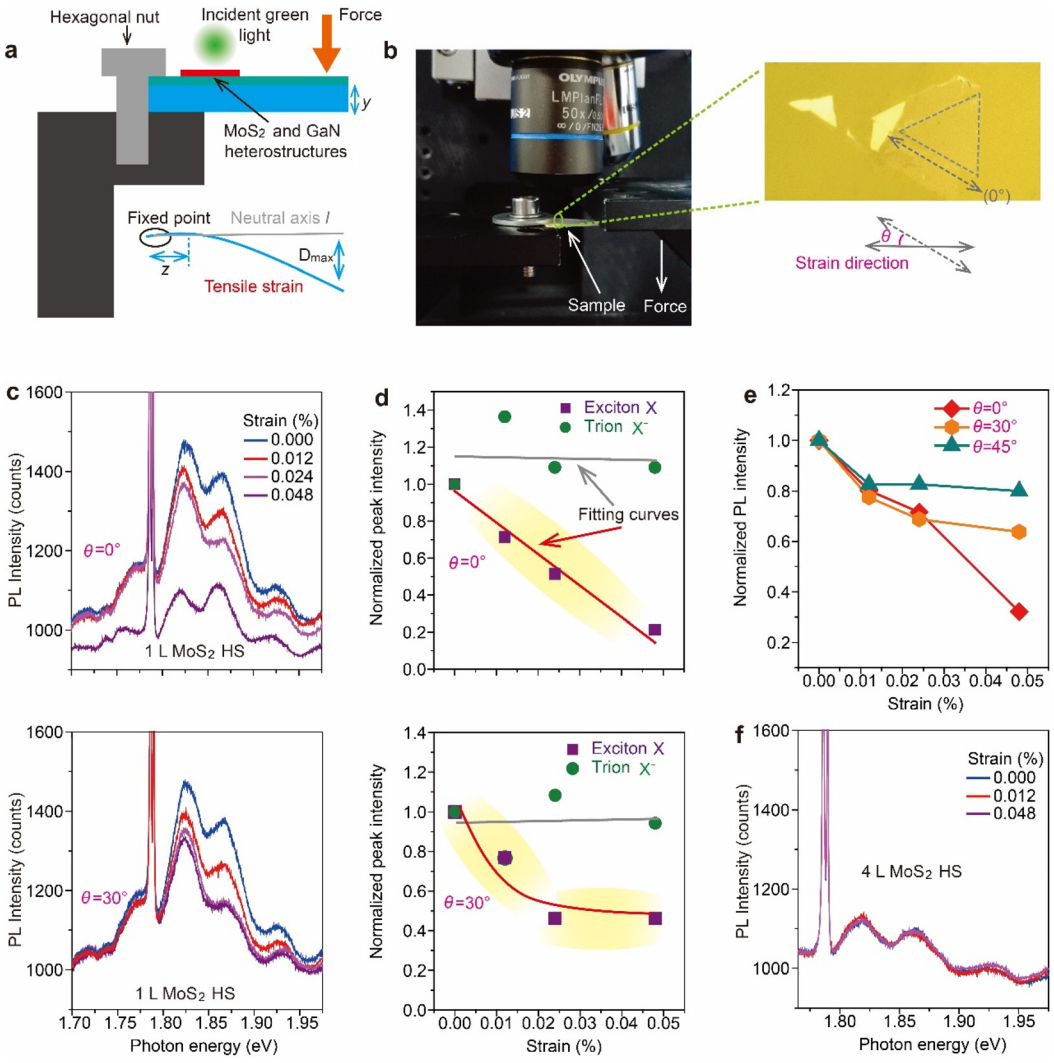


**Fig. 3** PL intensity of monolayer-$MoS_2$/GaN heterostructures as a function of tensile strain. (a) Schematic cross-sectional view and (b) practical microscopy of our testing set-up. A 3D stage was employed to apply external forces on the substrates for introducing tensile strain on the heterostructure as the red arrow indicates. One edge of monolayer $MoS_2$ is defined as 0° for the tensile strains (the inset of (b)). (c) PL responses to a function of the applied strains on monolayer-$MoS_2$/GaN heterostructures with the strain directions of 0° and 30°, respectively. As the strain increases, both the PL intensities remarkably decrease. (d) The changes in optical excitons and trions with respect to the applied strains. (e) Quantitative comparison of the relationships between PL peak intensities and tensile strains in different strain directions. The PL intensities at the directions of 0°, 30°, and 45° are normalized by the corresponding peaks without tensile strain. (f) PL spectra related to the applied strains for 4-layer-$MoS_2$/GaN heterostructures. Owing to the absence of the piezoelectric effect on 4-layer $MoS_2$, there is no obvious change in the PL responses.

contact with the rigid sapphire and the strain can be well transmitted to the sample. To quantify photoexcited dynamics upon the application of strains, it is necessary to fit the raw PL spectra in Fig. 3c with smooth curves using the Lorentzian function (Fig. S6†) and then de-convolute those fitting curves to demonstrate the variations of optically induced excitons and trions (Fig. 3d). As for the strain direction of 0°, when the strain magnitude is increased, the peak intensity of trion $X^-$ shows no obvious changing trends as the grey fitting line indicates, yet the peak intensity of exciton X rapidly decreases in a linear relationship with strains. In the case of 30°, the variation in trions also shows no obvious change, while that of exciton X first decreases and then reaches saturation.

To sum up, for vertically stacked heterostructures, when suffering tensile strains, the weight of excitons shows remarkable reduction but the weight of trions remains unchanged. Fig. 3e systematically depicts the normalized PL intensities as a function of the applied strain directions for monolayer-$MoS_2$/GaN heterostructures. Upon applying a small strain, the peak variation at different strain directions is almost identical. However, upon applying a large strain, the variation exhibits discrepancies arising from the angle-dependent piezoelectric field in monolayer $MoS_2$ (see Fig. 5 for more details): PL intensity at 0° rapidly decreases but the intensities at 30° and 45° slowly drop with different rates. In contrast, 4-layer-$MoS_2$/GaN heterostructures (Fig. 3f) demonstrate weak PL signals and no dependence on strains.

With regard to another emission peak (~2.84 eV, dominated by GaN films) from monolayer-$MoS_2$/GaN heterostructures (Fig. 4a) and separate GaN films (Fig. S7†), the applied strains have no obvious impact on the relevant PL spectra. This validates that the strain-induced piezoelectric field in the GaN film would not affect optical recombination. As discussed in Fig. 3, once $MoS_2$/GaN stacking forms, photoexcited dynamic responses at 1.75–1.95 eV are predominately determined by $MoS_2$ flakes. Therefore, considering the angle dependence of the quenched PL responses in monolayer-$MoS_2$/GaN stacking and the almost unchanged PL signals in the four-layer-$MoS_2$/GaN stacking, we attribute this quenched behavior to intrinsic $MoS_2$ piezoelectricity. Furthermore, we also obtained the suppressed PL intensity from flexible $MoS_2$ devices, in which monolayer $MoS_2$ was directly transferred on the PET substrates. Fig. 4b shows a typical optical microscopic image of monolayer $MoS_2$ and the inset displays a pertinent practical flexible device. Fig. 4c presents the PL spectra of a monolayer $MoS_2$ flake on the flexible PET substrate with respect to tensile strains. With the increase in the strain magnitude, PL spectra exhibit quenching responses and a slight red shift, suggesting that without heterostructure stacking (the piezoelectricity in the GaN film) the observed behaviors still exist. The documented work with SU8 as a flexible substrate reported that, as the strains were applied, monolayer $MoS_2$ showed a significant decrease in the PL intensity while the PL intensity of the bilayer was indeed strain independent.[49] The authors attribute this quenching phenomenon to strain-induced transformation between direct and indirect optical band gaps in monolayer $MoS_2$.

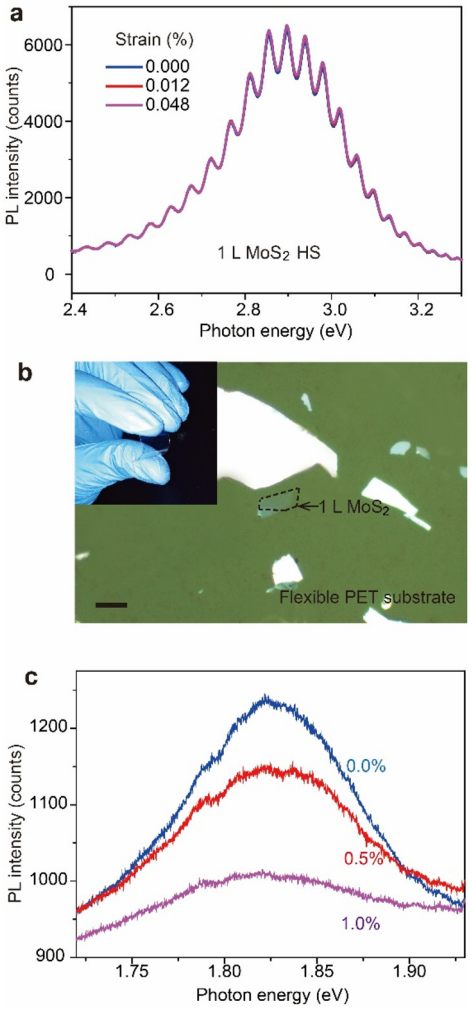


**Fig. 4** Contrastive experiments to confirm that the quenched responses result from the $MoS_2$ piezoelectricity in heterostructures. (a) PL spectra dominated by GaN films under different applied strains for monolayer-$MoS_2$/GaN heterostructures. As the magnitude of the external strain increases, the related emission peaks show no obvious change. (b) Optical microscopy of monolayer $MoS_2$ on a flexible PET substrate. The inset shows a typical flexible device. Scale bar: 10 μm. (c) PL spectra with respect to different applied tensile strains for the mentioned flexible device in (b). The quenched response is also observed, manifesting that the piezoelectricity in the $MoS_2$ flake governs the photo-excited process.

Nonetheless, a key question arises: how do the applied strains affect the optical-bandgap transformation? Here, as for either flexible monolayer $MoS_2$ devices or our $MoS_2$/GaN heterostructures, we propose that piezoelectricity in monolayer $MoS_2$ regulates the transformation (*i.e.*, decreased PL behaviors).

## Interpretation of the underlying physics

Fig. 5 elucidates how the piezoelectricity in $MoS_2$ flakes influences the optical recombination dynamics of monolayer-$MoS_2$/

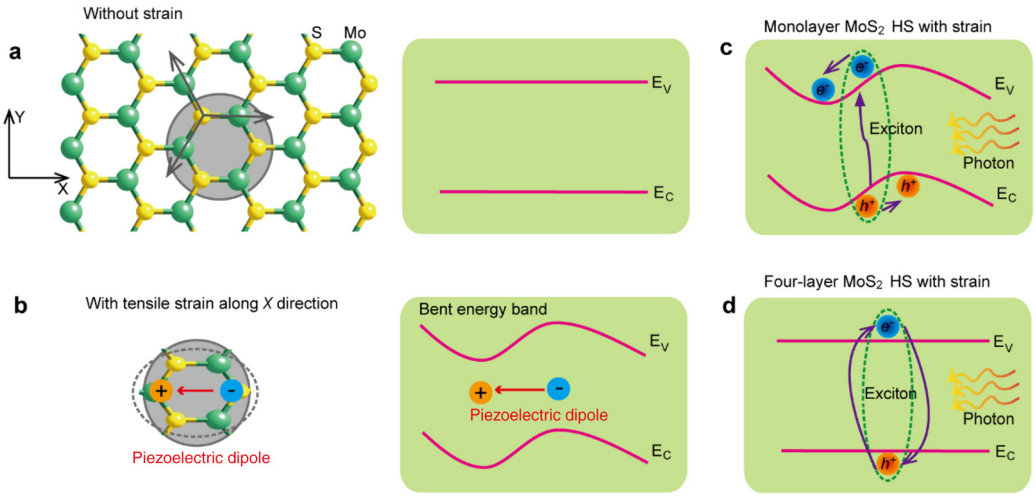


**Fig. 5** Crystal structure and band diagrams to interpret the underlying physics for the quenched PL responses. (a) Hexagonal crystal structure of monolayer $MoS_2$ viewing from the top without strain, and the relevant energy band. The directions of *x* and *y* denote 'armchair' and 'zigzag' edges of $MoS_2$, respectively. The piezoelectric field exists along the direction pointing from the S site to the Mo site, namely, the $e_{11}$ direction as indicated by grey arrows. (b) As the semiconductor is elongated, the tensile stress in the *x* direction and the compressive stress in the *y* direction are created, simultaneously resulting in the displacement of the Mo and S atoms and producing a net piezoelectric dipole as indicated by the red arrow. The immobile positive and negative ions among the piezoelectric dipole will make the bands bend downward and upward. Superposition of the generated net Mo–S piezoelectric dipoles along the *X* direction gives rise to a strong piezoelectric field. (c) Due to the inherent piezoelectric field, optical excitons will dissociate into spatially separated e–h quasi-particles and be stored in the bent energy band. (d) No modulation under applied strains in the absence of the piezoelectricity for four-layer $MoS_2$ heterostructures.

GaN heterostructures or separate monolayer $MoS_2$. The hexagonal crystal structure of monolayer $MoS_2$ and the relevant simplified energy band structure are shown in Fig. 5a. We define the *x* and *y* directions along the 'armchair' and 'zigzag' edges of monolayer $MoS_2$, respectively. In principle, as the solid grey arrows indicated, the produced piezoelectric fields point from S to Mo sites in the *xy* plane, namely, the $e_{11}$ direction.[28,29] A hexagonal structural unit is chosen for analysis, as indicated by the big grey circle highlighted in Fig. 5a. When applying a tensile strain along the *x* direction, the unit suffers a deformation: tensile stress in *x* and compressive stress in *y* are created. Meanwhile, Mo and S atoms produce relative displacements and piezoelectric dipoles.[50] These dipoles along the *x* direction are superimposed, whereas those along other directions offset each other. Therefore, net piezoelectric dipoles can be generated, which orient from the negative S site to the positive Mo site, as shown in the left-hand side image of Fig. 5b.

In the right-hand side image of Fig. 5b, within a piezoelectric dipole, the immobile positive ion attracts the free electrons across the monolayer $MoS_2$ to aggregate around it, leading to a decrease in the electrical potential energy and bandgap; in contrast, the negative ion compels the free electrons to move away from the dipole, resulting in an increase in the electrical potential energy and bandgap. Additionally, a strong piezoelectric field introduced by the net piezoelectric dipole moment along the direction of the applied tensile strain (*x* direction) can appear, which constitutes a driving force for the dissociation of tightly bound excitons. When a ray of laser is applied on the strained monolayer-$MoS_2$/GaN heterostructures (or $MoS_2$ flexible devices), a majority of optically induced excitons will dissociate, spatially separate, and be stored in the maxima and minima of valence and conduction bands, as displayed in Fig. 5c. This can explain the observed decrease in PL intensity. Because of the periodic piezoelectric field as indicated in Fig. 5a, the samples exhibit different strain tuning effects at different orientations, as shown in Fig. 3e. However, when removing the applied strains, this piezoelectric modulation effect disappears (Fig. S8†), clearly demonstrating that temporarily separated electron–hole pairs (quasi-particles) exist and will recover to recombination excitons. Because of the lack of piezoelectricity in the four-layer $MoS_2$, the applied strain does not have any influence on the energy band of $MoS_2$ (Fig. 5d), and thus the PL responses for the four-layer-$MoS_2$/GaN heterostructures.

In conclusion, we have investigated piezoelectricity-tuned optical dynamics of atom-thick-$MoS_2$ and thin-film-GaN heterostructures. With the increase in temperatures, all Raman active modes and PL spectra show a red shift, yet the PL intensities show a decrease due to the thermal expansion. As the magnitude of the applied tensile strain increases, the corresponding PL spectra show quenched responses mainly associated with the markedly decreased weight of exciton X. We ascribe this phenomenon to the piezoelectricity in monolayer $MoS_2$. Within strain-induced piezoelectric dipoles, the positive and negative immobile ions can render $MoS_2$ energy bands bending downward and upward, respectively. Consequently, a majority of optically induced excitons will spatially separate and then store in the maxima and minima of valence and conduction bands, thereby resulting in our observed behaviors. In addition, because of the lateral periodic

piezoelectricity in $MoS_2$ flakes, the changing trend of PL emission peaks can be determined by strain directions.

We believe that strain is a general approach to tune optical recombination dynamics *via* the piezoelectric effect[51] and can be applied to other material systems, such as 2D piezoelectric SnS and ZnO.[52,53] This work not only helps in interpreting the underlying mechanism of strain-dependent PL spectra of piezoelectric materials, but also provides a technical route to control the performances of optoelectronics by strain and develop tactile adaptive optoelectronics.

## Experimental methods

### Preparation of $MoS_2$/GaN heterostructures

$MoS_2$ samples were exfoliated from bulk crystals (bought from SPI) using mechanical methods and then transferred onto silicon substrates with 300 nm silica layers. After identifying the thicknesses by optical microscopy and Raman spectra, the chosen samples were transferred to GaN films grown on a sapphire substrate, using the wet chemical method as follows. First, PMMA (A3) was uniformly coated on the samples and baked at 170 °C for 10 min. Second, the KOH solution with a mass concentration of 10% was heated to 80 °C for boosting the etching rate of the oxide layer. Meanwhile, the samples covered with PMMA were soaked in the prepared KOH solution. Third, when floating on the top surface of deionized water, the PMMA layers, carried with target samples, were slowly picked up and successfully transferred to GaN films. Fourth, the sacrificed PMMA layers were dissolved in acetone. Note that the p-type GaN films, with thicknesses of 4–5 μm, were Mg-doped and grown by the MOCVD method with a carrier density of $6 \times 10^{16}$ $cm^{-3}$.

### Raman and PL measurements

The temperature testing setup was a HFS600E-PB4 temperature-controlled probe stage brought from Linkam Scientific Instruments. The Raman and PL spectra were measured using a Horiba LABRAM-HR evolution microscope. The experimental data in Fig. 2a and b were collected using a short-focus objective lens (100×) to ensure that the CCD can receive more emission photons from the samples. A UV objective lens (40×) was employed to obtain the data shown in Fig. 2f, and a long-focus objective lens (50×) was used to conduct the rest of the experiments for conveniently applying the variations in temperature and strain. The 532 nm laser with a power of 6 mW was used to perform the Raman characterizations and related PL responses. In addition, a UV laser with a 325 nm wavelength was employed to excite the GaN films as shown in Fig. 2f.

### Estimation of the strain induced in $MoS_2$ and GaN heterostructures

Due to the strong van der Waals forces between atomically thin $MoS_2$ and GaN films, the $MoS_2$ flake will follow the deformations of the GaN substrates under the applied strains. The applied tensile strain ($\varepsilon$) can be estimated using the following equation:[28]

$$\varepsilon = \frac{3y}{l}\frac{D_{max}}{l}\left(1 - \frac{z}{l}\right)$$

where $y$, $l$, $z$ and $D_{max}$ are all labeled in Fig. 3a.

## Data availability

The data supporting the findings of this study are available within the article and the supplementary files are available from the authors upon reasonable request.

## Conflicts of interest

The authors declare no competing interests.

## Acknowledgements

This research was supported by the ZJU-Hangzhou Global Scientific and Technological Innovation Center with a startup funding (02170000-K02013012).

## References

1 R. Ganatra and Q. Zhang, *ACS Nano*, 2014, **8**, 4074–4099.
2 K. F. Mak, C. Lee, J. Hone, J. Shan and T. F. Heinz, *Phys. Rev. Lett.*, 2010, **105**, 136805.
3 A. Chernikov, T. C. Berkelbach, H. M. Hill, A. Rigosi, Y. Li, B. Aslan, D. R. Reichman, M. S. Hybertsen and T. F. Heinz, *Phys. Rev. Lett.*, 2014, **113**, 076802.
4 S. Mouri, Y. Miyauchi and K. Matsuda, *Nano Lett.*, 2013, **13**, 5944–5948.
5 H. Nan, Z. Wang, W. Wang, Z. Liang, Y. Lu, Q. Chen, D. He, P. Tan, F. Miao, X. Wang, J. Wang and Z. Ni, *ACS Nano*, 2014, **8**, 5738–5745.
6 M. Amani, D.-H. Lien, D. Kiriya, J. Xiao, A. Azcatl, J. Noh, S. R. Madhvapathy, R. Addou, K. C. Santosh, M. Dubey, K. Cho, R. M. Wallace, S.-C. Lee, J.-H. He, J. W. Ager III, X. Zhang, E. Yablonovitch and A. Javey, *Science*, 2015, **350**, 1065–1068.
7 D.-H. Lien, S. Z. Uddin, M. Yeh, M. Amani, H. Kim, J. W. Ager III, E. Yablonovitch and A. Javey, *Science*, 2019, **364**, 468–471.
8 Y. Yamada, K. Shinokita, Y. Okajima, S. N. Takeda, Y. Matsushita, K. Takei, T. Yoshimura, A. Ashida, N. Fujimura, K. Matsuda and D. Kiriya, *ACS Appl. Mater. Interfaces*, 2020, **12**, 36496–36504.
9 D.-S. Tsai, K.-K. Liu, D.-H. Lien, M.-L. Tsai, C.-F. Kang, C.-A. Lin, L.-J. Li and J.-H. He, *ACS Nano*, 2013, **7**, 3905–3911.
10 O. Lopez-Sanchez, D. Lembke, M. Kayci, A. Radenovic and A. Kis, *Nat. Nanotechnol.*, 2013, **8**, 497–501.
11 Y. Pang, F. Xue, L. Wang, J. Chen, J. Luo, T. Jiang, C. Zhang and Z. L. Wang, *Adv. Sci.*, 2016, **3**, 1500419.

 

12 G. A. Saenz, G. Karapetrov, J. Curtis and A. B. Kaul, *Sci. Rep.*, 2018, **8**, 1276.
13 H.-Y. Lan, Y.-H. Hsieh, Z.-Y. Chiao, D. Jariwala, M.-H. Shih, T.-J. Yen, O. Hess and Y.-J. Lu, *Nano Lett.*, 2021, **21**, 3083–3091.
14 N. Li, C. He, Q. Wang, J. Tang, Q. Zhang, C. Shen, J. Tang, H. Huang, S. Wang, J. Li, B. Huang, Z. Wei, Y. Guo, J. Yuan, W. Yang, R. Yang, D. Shi and G. Zhang, *Nano Res.*, 2022, **15**, 5418–5424.
15 Y. Li, L. Li, S. Li, J. Sun, Y. Fang and T. Deng, *ACS Omega*, 2022, **7**, 13615–13621.
16 M.-L. Tsai, S.-H. Su, J.-K. Chang, D.-S. Tsai, C.-H. Chen, C.-I. Wu, L.-J. Li, L.-J. Chen and J.-H. He, *ACS Nano*, 2014, **8**, 8317–8322.
17 S. Wi, H. Kim, M. Chen, H. Nam, L. J. Guo, E. Meyhofer and X. Liang, *ACS Nano*, 2014, **8**, 5270–5281.
18 C.-J. Park, H. J. Park, J. Y. Lee, J. Kim, C.-H. Lee and J. Joo, *ACS Appl. Mater. Interfaces*, 2018, **10**, 29848–29856.
19 K. M. Islam, T. Ismael, C. Luthy, O. Kizilkaya and M. D. Escarra, *ACS Appl. Mater. Interfaces*, 2022, **14**, 24281–24289.
20 Y. Ye, Z. Ye, M. Gharghi, H. Zhu, M. Zhao, Y. Wang, X. Yin and X. Zhang, *Appl. Phys. Lett.*, 2014, **104**, 193508.
21 M. Choi, Y. J. Park, B. K. Sharma, S.-R. Bae, S. Y. Kim and J.-H. Ahn, *Sci. Adv.*, 2018, **4**, eaas8721.
22 Y. Woo, W. Hong, S. Y. Yang, H. J. Kim, J.-H. Cha, J. E. Lee, K. J. Lee, T. Kang and S.-Y. Choi, *Adv. Electron. Mater.*, 2018, **4**, 1800251.
23 H. Kwon, S. Garg, J. H. Park, Y. Jeong, S. Yu, S. M. Kim, P. Kung and S. Im, *npj 2D Mater. Appl.*, 2019, **3**, 9.
24 M. Choi, S.-R. Bae, L. Hu, H. Anh Tuan, S. Y. Kim and J.-H. Ahn, *Sci. Adv.*, 2020, **6**, eabb5898.
25 A. Alarawi, V. Ramalingam, H. C. Fu, P. Varadhan, R. S. Yang and J. H. He, *Opt. Express*, 2019, **27**, A352–A363.
26 A. Alarawi, V. Ramalingam and J.-H. He, *Mater. Today Energy*, 2019, **11**, 1–23.
27 K.-A. N. Duerloo, M. T. Ong and E. J. Reed, *J. Phys. Chem. Lett.*, 2012, **3**, 2871–2876.
28 W. Wu, L. Wang, Y. Li, F. Zhang, L. Lin, S. Niu, D. Chenet, X. Zhang, Y. Hao, T. F. Heinz, J. Hone and Z. L. Wang, *Nature*, 2014, **514**, 470–474.
29 H. Zhu, Y. Wang, J. Xiao, M. Liu, S. Xiong, Z. J. Wong, Z. Ye, Y. Ye, X. Yin and X. Zhang, *Nat. Nanotechnol.*, 2015, **10**, 151–155.
30 W. Wu, L. Wang, R. Yu, Y. Liu, S.-H. Wei, J. Hone and Z. L. Wang, *Adv. Mater.*, 2016, **28**, 8463–8468.
31 Y. Zhang, W. Jie, P. Chen, W. Liu and J. Hao, *Adv. Mater.*, 2018, **30**, 1707007.
32 A. R. Rezk, B. Carey, A. F. Chrimes, D. W. M. Lau, B. C. Gibson, C. Zheng, M. S. Fuhrer, L. Y. Yeo and K. Kalantar-zadeh, *Nano Lett.*, 2016, **16**, 849–855.
33 M. Moun, M. Kumar, M. Garg, R. Pathak and R. Singh, *Sci. Rep.*, 2018, **8**, 11799.
34 A. Quellmalz, X. Wang, S. Sawallich, B. Uzlu, M. Otto, S. Wagner, Z. Wang, M. Prechtl, O. Hartwig, S. Luo, G. S. Duesberg, M. C. Lemme, K. B. Gylfason, N. Roxhed, G. Stemme and F. Niklaus, *Nat. Commun.*, 2021, **12**, 917.
35 P. Wang, C. Jia, Y. Huang and X. Duan, *Matter*, 2021, **4**, 552–581.
36 D. Li, R. Cheng, H. Zhou, C. Wang, A. Yin, Y. Chen, N. O. Weiss, Y. Huang and X. Duan, *Nat. Commun.*, 2015, **6**, 7509.
37 M. C. Lemme, D. Akinwande, C. Huyghebaert and C. Stampfer, *Nat. Commun.*, 2022, **13**, 1392.
38 F. Xue, L. Chen, J. Chen, J. Liu, L. Wang, M. Chen, Y. Pang, X. Yang, G. Gao, J. Zhai and Z. L. Wang, *Adv. Mater.*, 2016, **28**, 3391–3398.
39 P. Gupta, A. A. Rahman, S. Subramanian, S. Gupta, A. Thamizhavel, T. Orlova, S. Rouvimov, S. Vishwanath, V. Protasenko, M. R. Laskar, H. G. Xing, D. Jena and A. Bhattacharya, *Sci. Rep.*, 2016, **6**, 23708.
40 W. Limmer, W. Ritter, R. Sauer, B. Mensching, C. Liu and B. Rauschenbach, *Appl. Phys. Lett.*, 1998, **72**, 2589–2591.
41 D. Ruzmetov, K. Zhang, G. Stan, B. Kalanyan, G. R. Bhimanapati, S. M. Eichfeld, R. A. Burke, P. B. Shah, T. P. O'Regan, F. J. Crowne, A. G. Birdwell, J. A. Robinson, A. V. Davydov and T. G. Ivanov, *ACS Nano*, 2016, **10**, 3580–3588.
42 L. Chen, F. Xue, X. Li, X. Huang, L. Wang, J. Kou and Z. L. Wang, *ACS Nano*, 2016, **10**, 1546–1551.
43 F. Xue, L. Chen, L. Wang, Y. Pang, J. Chen, C. Zhang and Z. L. Wang, *Adv. Funct. Mater.*, 2016, **26**, 2104–2109.
44 S. Sahoo, A. P. S. Gaur, M. Ahmadi, M. J.-F. Guinel and R. S. Katiyar, *J. Phys. Chem. C*, 2013, **117**, 9042–9047.
45 K. F. Mak, K. He, C. Lee, G. H. Lee, J. Hone, T. F. Heinz and J. Shan, *Nat. Mater.*, 2013, **12**, 207–211.
46 J. Zhang, J. Wang, P. Chen, Y. Sun, S. Wu, Z. Jia, X. Lu, H. Yu, W. Chen, J. Zhu, G. Xie, R. Yang, D. Shi, X. Xu, J. Xiang, K. Liu and G. Zhang, *Adv. Mater.*, 2016, **28**, 1950–1956.
47 M. Buscema, G. A. Steele, H. S. J. van der Zant and A. Castellanos-Gomez, *Nano Res.*, 2014, **7**, 561–571.
48 N. Ben Sedrine, T. C. Esteves, J. Rodrigues, L. Rino, M. R. Correia, M. C. Sequeira, A. J. Neves, E. Alves, M. Bockowski, P. R. Edwards, K. P. O'Donnell, K. Lorenz and T. Monteiro, *Sci. Rep.*, 2015, **5**, 13739.
49 H. J. Conley, B. Wang, J. I. Ziegler, R. F. Haglund Jr., S. T. Pantelides and K. I. Bolotin, *Nano Lett.*, 2013, **13**, 3626–3630.
50 Z. L. Wang and J. Song, *Science*, 2006, **312**, 242–246.
51 H. Chen, Z. Dong, Y. Zhao, S. Li, X. Du, Z. Wu, W. Liu and Y. Zhang, *J. Lumin.*, 2020, **219**, 116914.
52 H. Khan, N. Mahmood, A. Zavabeti, A. Elbourne, M. A. Rahman, B. Y. Zhang, V. Krishnamurthi, P. Atkin, M. B. Ghasemian, J. Yang, G. Zheng, A. R. Ravindran, S. Walia, L. Wang, S. P. Russo, T. Daeneke, Y. Li and K. Kalantar-Zadeh, *Nat. Commun.*, 2020, **11**, 3449.
53 N. Mahmood, H. Khan, K. Tran, P. Kuppe, A. Zavabeti, P. Atkin, M. B. Ghasemian, J. Yang, C. Xu, S. A. Tawfik, M. J. S. Spencer, J. Z. Ou, K. Khoshmanesh, C. F. McConville, Y. Li and K. Kalantar-Zadeh, *Mater. Today*, 2021, **44**, 69–77.